Controlled Intracellular Polymerization for Cancer Treatment

JACS Au
AN OPEN ACCESS JOURNAL OF THE AMERICAN CHEMICAL SOCIETY

pubs.acs.org/jacsau

Article

Controlled Intracellular Polymerization for Cancer Treatment

Yichuan Zhang,[‖] Quan Gao,[‖] Weishuo Li, Rongkun He, Liwei Zhu, Qianjin Lian, Liang Wang, Yang Li, Mark Bradley, and Jin Geng*

Cite This: *JACS Au* 2022, 2, 579–589

Read Online

ACCESS | Metrics & More | Article Recommendations | Supporting Information

ABSTRACT: Numerous prodrugs have been developed and used for cancer treatments to reduce side effects and promote efficacy. In this work, we have developed a new photoactivatable prodrug system based on intracellular photoinduced electron transfer–reversible addition–fragmentation chain-transfer (PET–RAFT) polymerization. This unique polymerization process provided a platform for the synthesis of structure-predictable polymers with well-defined structures in living cells. The intracellularly generated poly(*N*,*N*-dimethylacrylamide)s were found to induce cell cycle arrest, apoptosis, and necroptosis, inhibit cell proliferation, and reduce cancer cell motilities. This polymerization-based "prodrug" system efficiently inhibits tumor growth and metastasis both *in vitro* and *in vivo* and will promote the development of targeted and directed cancer chemotherapy.

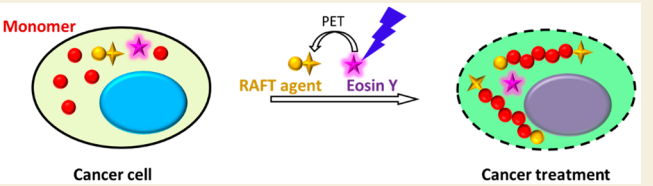

KEYWORDS: *Intracellular polymerization, Photoinduced polymerization, Reversible addition–fragmentation chain-transfer polymerization, Apoptosis, Cell cycle arrest, Tumor metastasis inhibition, Cancer treatment*

INTRODUCTION

Current cancer treatments include surgical intervention, radiotherapy, and chemotherapy. Although chemotherapy is highly efficient, it often causes severe toxicity and side effects. It would therefore be desirable to develop chemotherapeutics that can target and be activated in/on cancerous cells. Prodrugs, chemically modified drug molecules that release pharmacologically active drugs upon transformation *in vivo*, are attractive therapeutic agents.[1−4] Typically, for cancer treatment, prodrugs are chemically modified anticancer agents that shield their toxicities and therefore can minimize the required dosage and reduce adverse side effects to patients.[5,6] Stimuli for prodrug activations include internal and external triggers, e.g., overexpressed enzymes,[7] subphysiological pH,[8] hypoxia,[9] and reducing and oxidizing agents.[10,11] External inputs need to be artificially introduced to the biological system, including light,[12] ultrasound,[13] and synthetic molecules.[14] In comparison to internal triggers, external stimuli offer precise spatial and temporal control over the site of action. For example, light is a highly controllable energy source[15−17] and has been used to control microtubule dynamics via a photoswitchable microtubule inhibitor for cancer treatment,[18] while a photocleavable linker was introduced between a proteasome inhibitor and doxorubicin, allowing two anticancer agents to be simultaneously "activated" upon illumination.[19]

Photoinduced polymerization is well-developed and has been used in a number of biological and medical applications, such as for generation of coatings (e.g., catheters) and scaffolds;[20−22] however, the introduction of such powerful chemical tools inside cells has been rarely explored. Wang et al. reported the enzyme-mediated polymerization and self-assembly of peptides in cells as potential cancer diagnostics and therapeutics.[23,24] Hawker et al. reported a strategy for synthesizing unnatural polymers on the surface of yeast via photoinitiated polymerization.[25] Recently, we demonstrated the photoinitiated free radical polymerization in living cells[26] with polymers, such as poly(*N*-(2-hydroxypropyl)-methacrylamide) and poly(sodium 4-styrenesulfonate), generated in cells, modulating cellular function and behavior without affecting cell viability.

Typically, substances introduced into biological systems need to have chemically defined compositions and chemical structures.[27,28] Conventional free radical polymerizations lack the control over molecular weight, therefore limiting their reproducibility and potential in biomedical applications.[29] Owing to the unique energy transfer mechanism, photoinduced electron transfer–reversible addition–fragmentation chain-transfer (PET–RAFT) polymerization offers a controlled polymerization progress giving polymers with predictable molecular weights and narrow dispersities in biologically relevant environments (i.e., at room temperature in the presence of water and oxygen).[25] In addition, oxygen-tolerant,

Received: August 26, 2021
Published: February 23, 2022

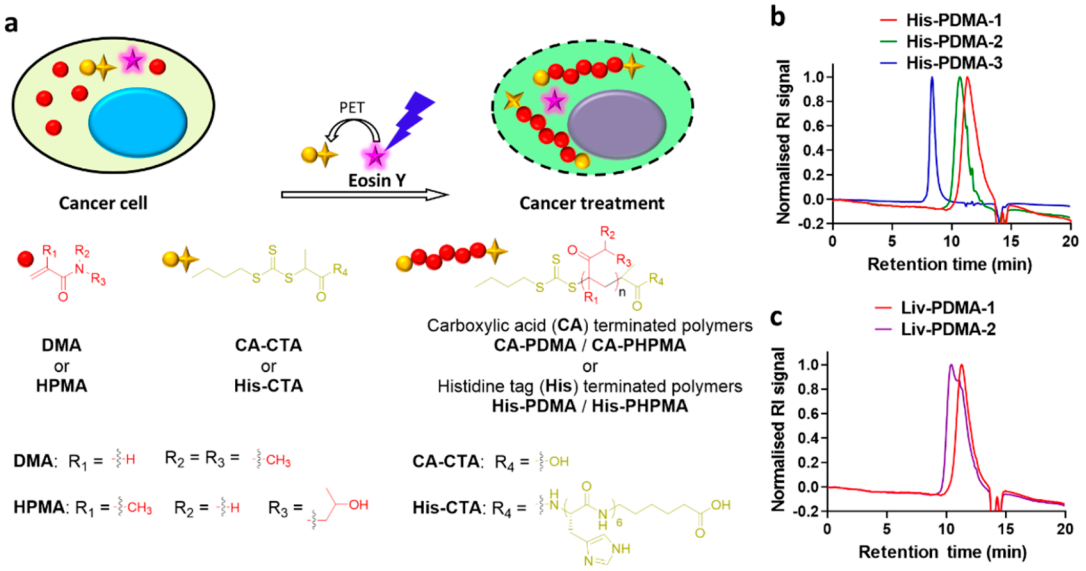

Figure 1. Intracellular PET−RAFT polymerization. (a) Schematic illustration of the intracellular polymerization. (b) GPC traces of the isolated **His-PDMA-1**, **His-PDMA-2**, and **His-PDMA-3** and (c) **Liv-PDMA-2** and **Liv-PDMA-1**. PET−RAFT polymerization was conducted in cells using a hexahistidine-tagged **His-CTA**. The intracellularly synthesized polymers were obtained by dialysis (MWCO = 1000 Da) and IMAC isolation.

organic-fluorophore-based initiating systems have been developed for RAFT polymerizations using visible light as the energy source and are compatible for biological applications.[30,31]

In this study, an intracellular polymerization-based "prodrug" system is developed and used for cancer treatment. We found that monomers, such as *N*,*N*-dimethylacrylamide (DMA), had tunable cytotoxicity with cells upon visible-light-mediated intracellular RAFT polymerization. We observed that the generation of poly(DMA) inside tumor cells could induce cell cycle arrest, apoptosis, and necroptosis as well as reduce cell proliferation and motility. Importantly, we observed that intracellular polymerization significantly reduced tumor growth and metastasis *in vivo*. We hypothesize that using monomers as "prodrugs" and targeted polymerization inside cells could be a new strategy for cancer treatment, where a nontoxic monomer could be converted into an active polymeric form only at the site of illumination. Thus, the intracellular polymerization could offer a new modality within therapeutic oncology.

RESULTS AND DISCUSSIONS

Cellular Uptake and Intracellular Polymerization Condition Optimization

In a previous study, we observed that free radical polymerization took place inside cells but lacked the control over polymer structures generated (molecular weight dispersities, $Đ$ > 1.7).[26] Thus, we employed a visible-light-induced PET−RAFT polymerization to achieve a controlled polymerization process in this study. A typical PET−RAFT system consists of a monomer, a photosensitizer, and a chain-transfer agent (CTA). As previously reported, the chemical structure of CTAs greatly influences the stability of the radical/redox intermediates and thus the reaction rate and the dispersities of the resulting polymers.[32,33] We chose a trithiocarbonate-based CTA, as it is suitable for a wide range of monomers, including styrenes, acrylates, and methacrylates.[34−37]

Considering the need for aqueous solubility, **CA-CTA** with a short aliphatic chain and a carboxylic acid terminal group was synthesized and utilized here (Figure 1a).[38] **Eosin Y** was chosen as the photosensitizer owing to its high energy transfer efficiency and biocompatibility, and importantly, **eosin Y** is known to give polymers with low dispersities in a PET−RAFT polymerization.[39,40]

A visible light source (470 nm, 100 mW/cm^2, 2 cm beneath the reaction solution, see the reaction setup in Figure S9) was used to initiate the polymerization.[30] The cytotoxicities of **CA-CTA**, **eosin Y**, and the light were evaluated against HeLa cells, giving the optimized concentrations for **CA-CTA** (1.0 mM), **eosin Y** (100 μM), and an optimized illumination time of 10 min for the initiation of the intracellular polymerization (Figure S10).

A library of water-soluble acrylate/acrylamide derivatives was chosen, and their IC50s were determined against HeLa cells (Figure S11). Monomers *N*-(2-hydroxypropyl)-methacrylamide (**HPMA**, 50 mM), methacrylic acid (5 mM), **DMA** (5 mM), poly(ethylene glycol) methacrylate (1.0 mM), and 2-(diethylamino)ethyl methacrylate (1.0 mM) (at the highest concentrations where HeLa cells gave viabilities over 90%) were polymerized individually in PBS (pH = 7.4) in the presence of 1.0 mM **CA-CTA**, 100 μM **eosin Y**, and 10 min of illumination. We observed that both **HPMA** and **DMA** were polymerized, with conversions of 6 and 19%, respectively (Figure S12).

The cellular uptake of **DMA**, **HPMA**, **CA-CTA**, and **eosin Y** was subsequently quantified by UV−vis spectroscopy (Figure S13), and all components showed good cell penetration. All components were found stable in a biologically relevant environment (in serum, 37 °C, 72 h) (Figure S14). When we treated cells with **DMA** (5 mM), **HPMA** (50 mM), **CA-CTA** (1.0 mM), and **eosin Y** (100 μM) individually for 4 h, intracellular concentrations were found to be 52, 379, 1.8, and 0.18 fmol/cell, respectively. A fluorescent monomer **YFMA** [$\lambda_{ex/em}$ (**YFMA**) = 560/580 nm] and a fluorescent CTA **RF-CTA** [$\lambda_{ex/em}$ (**RF-CTA**) = 630/650 nm] were synthesized (see synthetic procedures and characterizations in Supporting

https://doi.org/10.1021/jacsau.1c00373
JACS Au 2022, 2, 579−589

Table 1. Polymers Synthesized inside Living Cells

	c (DMA) (mM)	c (HPMA) (mM)	c (His-CTA) (μM)	c (eosin Y) (μM)	M_n (kDa)[a]	Đ[a]
His-PDMA-1	5.0	-	1000.0	100.0	13.2	1.07
His-PDMA-2	5.0	-	500.0	50.0	17.4	1.12
His-PDMA-3	5.0	-	100.0	10.0	26.8	1.26
His-PHPMA-1	-	50.0	1000.0	100.0	20.9	1.11
His-PHPMA-2	-	50.0	500.0	50.0	32.2	1.19
His-PHPMA-3	-	50.0	100.0	10.0	53.6	1.33
Liv-PDMA-1	5.0	-	1000.0	100.0	13.2	1.08
Liv-PDMA-2[b]	5.0	-	-	100.0	17.9	1.29

[a] M_n and Đ were characterized by GPC using DMF as the eluent at a flow rate of 1 mL/min. [b] **Liv-PDMA-2** was polymerized intracellularly utilizing the *in-situ*-generated **Liv-PDMA-1** as a marco-RAFT-CTA.

Information) and coincubated with **DMA**, **CA-CTA**, and **eosin Y**. Colocalization of the fluorescent monomer, CTA, and **eosin Y** were confirmed using confocal microscopy (Figure S15). The subcellular location of the fluorescent monomer was confirmed by costaining with organelle markers, and its accumulation in mitochondria was observed (Figure S16).

HeLa cells were treated with our polymerization cocktails (**PC1** contains **DMA** 5 mM, **CA-CTA** 1.0 mM, and **eosin Y** 100 μM; **PC2** contains **HPMA** 50 mM, **CA-CTA** 1.0 mM, and **eosin Y** 100 μM) in DMEM, and the polymerization was initiated by illumination (all polymerizations were conducted by illumination at 470 nm for 10 min). The monomer conversions of **DMA** and **HPMA** in HeLa cells were quantified as 34 and 10%, respectively (Figure S17), which were similar to the polymerizations conducted in PBS under the same conditions (29 and 10%, respectively) (Figure S18). When we reduced the concentrations of **CA-CTA** from 1.0 mM to 100 μM, in the presence of **eosin Y** (0.1 equiv of **CA-CTA**) and **DMA** (5 mM), the monomer conversions reduced accordingly due to the reduced chain numbers (Figure S17).

Polymer Characterization

We explored the controlled intracellular polymerization progress using the polymers extracted from the "polymerized" cells using a hexahistidine-tagged CTA **His-CTA** allowing highly efficient polymer extraction via an immobilized metal-affinity chromatograph (IMAC) strategy (Figures S7 and S8).[41] Intracellular polymerization of **DMA** and **HPMA** with **His-CTA** was conducted under the same conditions as discussed above (Figure 1a). **His-PDMA-1** and **His-PHPMA-1** were isolated from the "polymerized" cells and analyzed by ^{1}HNMR and gel permeation chromatography (GPC) and compared to the polymers obtained from cells with those polymerized in PBS (pH = 7.4) (Figure S19). The series of His-PDMAs and His-PHPMAs successfully synthesized intracellularly had Đ values as narrow as 1.07, with similar molecular weights and dispersities observed as those synthesized in PBS, indicating a controlled polymerization (Figures 1b and S19 and Tables 1 and S1).

Copolymerization and Living Polymerization

We carried out the copolymerization of **DMA** with a biotinylated methacrylate monomer[31] under the same reaction conditions as described above. Here, the biotinylated copolymers were extracted from cells using streptavidin-functionalized magnetic nanoparticles. Again, the copolymers were found to have an extremely narrow Đ (1.03−1.06) when compared to those polymers obtained via free radical polymerization (Đ > 1.7) in our previous study,[31] indicating the successful controlled copolymerizations through the PET−RAFT process (Figure S20).

In addition, with the use of the fluorescent monomers **YFMA** and CTA **RF-CTA**, the resulting polymer can be "visualized" by a confocal microscope. We observed that the generated dual-fluorescent polymers (yellow and red) can be retained longer than the fluorescent monomers in cells where the polymerized cells exhibited a higher fluorescence intensity after 24 h (Figure S21). The observations further confirmed the successful intracellularly polymerization.

The "living" property of this system was investigated by a two-step polymerization in the same cells. First, HeLa cells were incubated with **PC1** for 4 h and polymerized for 10 min. The cells were harvested, and the polymer **Liv-PDMA-1** was isolated and characterized (molecular weight of 13.2 kDa and dispersity of 1.08). After 24 h, the "polymerized cells" (5×10^6), containing **Liv-PDMA-1**, were treated with another batch of **DMA** (5 mM) and **eosin Y** (100 μM) for 4 h and illuminated for 10 min. From the cells, **Liv-PDMA-2** was isolated and showed an increase in molecular weight (17.9 kDa) with a Đ of 1.29. The hypothesis is that living polymerization happened in the cells with **Liv-PDMA-1** acting as a macro-RAFT agent (Figures 1c and S22 and Table 1). Notably, a shoulder was observed in the GPC trace for **Liv-PDMA-2**, which could be attributed to the nonpropagated polymer, **Liv-PDMA-1**.

Intracellular Polymerization Induces Cytotoxicity to Cancer Cells

To investigate how the intracellular polymerization affected cell viabilities, we treated HeLa (human cervical adenocarcinoma), 4T1 (murine mammary carcinoma), MDA-MB-231 (human breast adenocarcinoma), MCF-7 (human breast adenocarcinoma), A375 (human malignant melanoma), 1205 Lu (human metastatic melanoma), HEK 293T (human embryonic kidney), and LO2 (human liver) cells with **PC1** and illumination. The polymerization of **DMA** inside cells induced a dramatically reduced cell viability for all cells (49% for HeLa, 40% for 4T1, 28% for MDA-MB-231, 12% for MCF-7, 21% for A375, and 60% for 1205 Lu cell) when compared to untreated cells (Figure S23). In addition, we observed that the polymerization of **DMA** through a free radical mechanism (initiated by photoinitiator BAPO) did not induce toxicities to cells (Figure S24). It is worth noting that when we treated cells with just **CA-CTA** (1.0 mM) and **eosin Y** (100 μM) in the absence of **DMA** with or without illumination, there was no effect on cell viability (Figure S25). A cross-linker *N*,*N*′-methylenebis(acrylamide) (**MBA**) has been introduced to the polymerization system to reveal how the molecular weights and dispersities of *in-situ*-synthesized polymers affect cell

https://doi.org/10.1021/jacsau.1c00373
JACS Au 2022, 2, 579−589

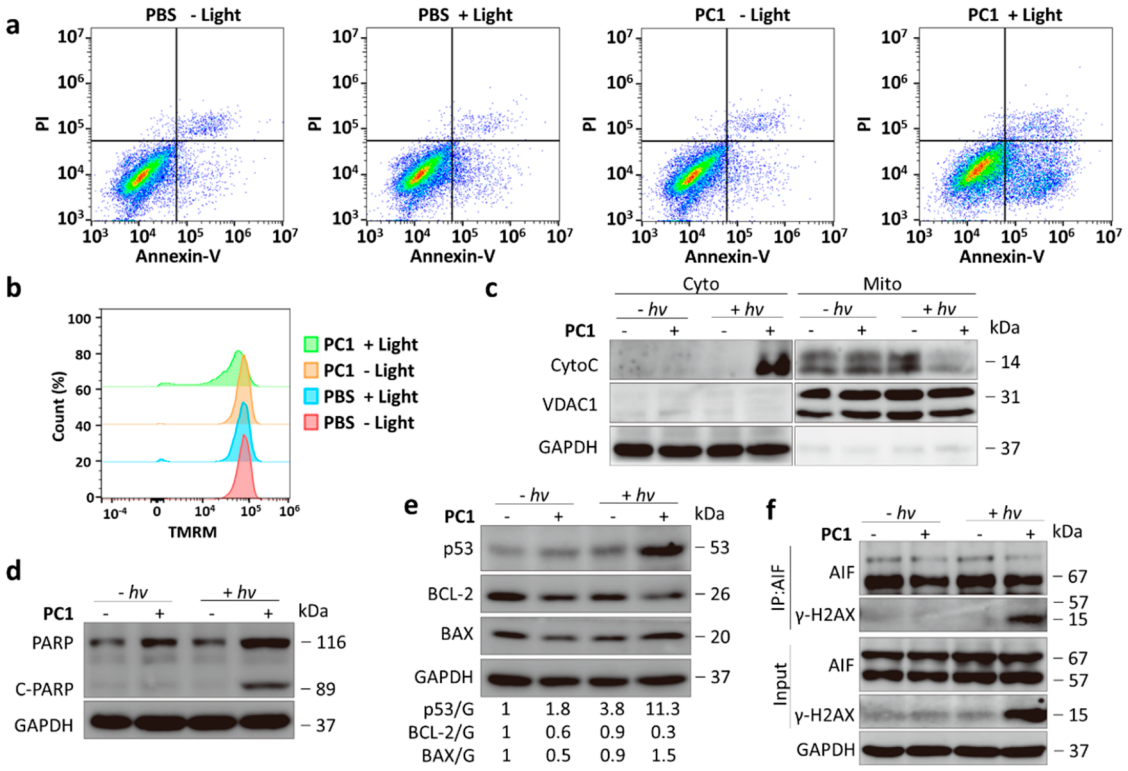

Figure 2. Intracellular polymerization induces programmed cell death. (a) The apoptosis and necroptosis induced by intracellular polymerization determined by flow cytometry. Apoptosis: Annexin-V-positive and PI-negative; necroptosis: PI-positive. (b) Mitochondrial membrane potential of HeLa cells evaluated by flow cytometry. (c–f) Key biological markers evaluated using immunoblotting and immunoprecipitation assays.

viabilities (Figure S26). In the presence of MBA, we observed that the cytotoxicities were promoted when the molecular weights and dispersities increase. The intracellular RAFT polymerization of **HPMA** did not induce cytotoxicity to HeLa cells with 97% viable cells compared to the untreated cells (Figure S27).

Intracellular Polymerization Induces Cancer Cell Apoptosis and Necroptosis

Having demonstrated the introduction of cytotoxicity to cancer cells by the intracellular polymerization of **DMA**, the mechanism was investigated. As reported before, numerous cancer therapeutics induce cytotoxic stress to cancer cells by ultimately triggering programmed cell death, which is related to the terms of apoptosis, necroptosis, and autography.[42,43] Translocation of phosphatidylserine is a standard marker for early apoptosis and thus was initially analyzed by flow cytometry (Figures 2a and S29).[44] HeLa cells treated with **PC1** gave a moderate increase in the apoptotic cell ratio (from 3 to 5%) when compared to untreated cells, while the ratio in the "polymerized" cells was remarkable higher (19%). On the other hand, propidium iodide (PI) staining revealed an increase in necroptosis in the "polymerized" cells (4 compared to 3% for untreated cells). Similar results were found for A375 cells, although necroptosis was more significant than apoptosis (Figure S29). Furthermore, we found that the introduction of the pan-caspase inhibitor Cbz-Val-fluoromethylketone (Z-V-FMK) and the necroptosis inhibitor necrostatin-1 (Nec-1) to the "polymerized" HeLa cells significantly improved ($P < 0.0001$) the survival rate (from 51 to 64 and 67%, respectively), thus confirming that apoptosis and necroptosis were induced by the intracellular polymerization (Figure S29d).

As discussed in the previous section, the polymerization components accumulated in mitochondria. We assume that the *in-situ*-generated polymers could affect mitochondria function and induce programmed cell death to cancerous cells. As expected, a remarkable reduction of mitochondrial membrane potential, release of cytochrome C, and decrease of ATP synthesis were observed, indicating the alternation of mitochondrial functions by the polymerization (Figures 2b,c and S30).

A series of apoptosis, necroptosis, and autophagy markers were further explored by immunoblotting analysis to look for further insight into the mechanism. Cleavage of PARP and overexpression of p53 are typically seen as regulators for apoptosis and were explored here (Figure 2d,e). A remarkably elevated expression of both PARP and cleaved-PARP (C-PARP) was only observed in the "polymerized" cells (negligible expressions of C-PARP were observed in all control groups), indicating the activation of the caspase-dependent apoptotic pathway.[45] Similarly, we observed a high level of p53 expression (Figure 2e) in the "polymerized" cells together with a suppressed expression of BCL-2 (an antiapoptotic protein) and an elevated expression of BAX (a proapoptotic protein).[46,47] Importantly, the expression of p53 can increase mitochondrial permeability and further activate the mitochondria-mediated apoptosis pathway.[11,48] The complexation of released cytochrome C with cleaved caspase 9 was detected by an immunoprecipitation assay confirming that the polymerized cells underwent a mitochondria-mediated apoptosis pathway (Figure S31). Therefore, we believe that the apoptosis was induced by at least two different biological pathways, i.e., a caspase-dependent and mitochondria-mediated apoptosis pathway.

https://doi.org/10.1021/jacsau.1c00373
JACS Au 2022, 2, 579–589

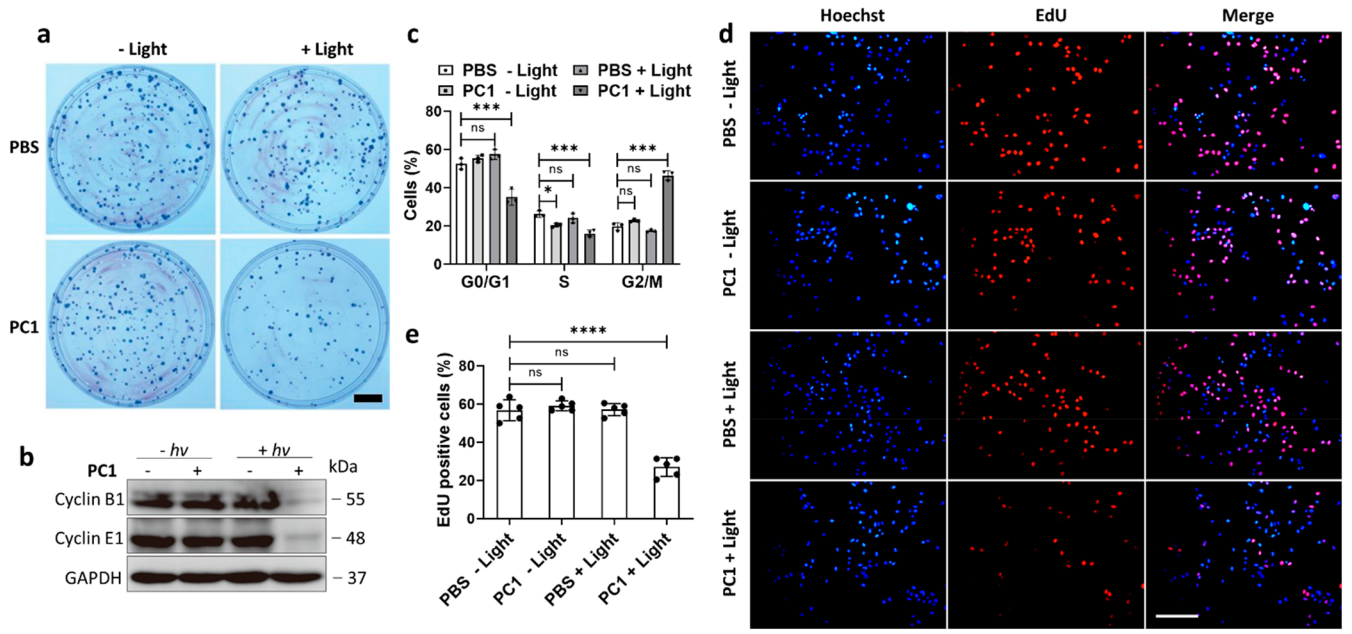

Figure 3. Intracellular polymerization induces cell cycle arrest and inhibits proliferation. (a) Colony growth assay revealing the proliferation ability of HeLa cells affected by intracellular polymerization. Scale bar represents 1 cm. (b) Key regulators of the cell cycle analyzed by an immunoblotting assay. (c) Cell cycle study of HeLa cells with or without intracellular polymerization (n = 6). (d) Cell proliferation study using an EdU staining assay. Scale bar = 50 μm. EdU-positive cells were counted, and the data are presented in (e) (n = 6). Statistical analysis was performed using one-way ANOVA with a Dunnett post-test compared to untreated control groups, * $P < 0.05$, *** $P < 0.001$, **** $P < 0.0001$, ns (not significant).

It is well-known that the nuclear translocation of AIF (apoptosis inducing factor) from the mitochondria mediates caspase-independent necroptosis.[49] Here, we found that intracellular polymerization promoted the expression of RIP1 (an AIF translocation promoter) together with a significant increase in AIF content in nuclei, while the overall level of AIF in the whole cell lysate was unchanged. The AIF−γ-H2AX complex formation was detected by an immunoprecipitation assay (Figure 2f). The generation of such a complex (not found in any control groups) indicated the necroptosis pathway induced by the intracellular polymerization.[50,51] These findings confirmed the translocation of AIF and the AIF-mediated caspase-independent necroptosis mechanism (Figure S32).

Autophagy, a highly conserved degradation mechanism in eukaryotic cells, is widely involved in cell growth, proliferation, development, tumor-cell invasion, and migration.[52] Immunoblotting analysis showed that intracellular polymerization significantly increased the expression of p62/SQSTM1, a selective substrate of autophagy, indicating the inhibition of the autophagy.[53] BECN1 and the Atg5−Atg12 complex are essential for autophagy initiation and thus were analyzed with a dramatic level of decreases observed (both BECN1/GAPDH and Atg5−Atg12/GAPDH ratio decrease from 1.0 to 0.6 for polymerized cells compared to untreated cells). As expected, intracellular polymerization increased the expression of LC3-II, a marker of autophagosome,[54] but the CQ addition (an inhibitor of autophagosome−lysosome fusion[55]) did not induce further accumulation of LC3-II, further confirming that autophagy was inhibited by the intracellular polymerization (Figure S33)

Intracellular Polymerization Inhibits Cancer Cell Proliferation

As previously discussed, high-level expression of p53 protein not only triggers apoptosis but also affects cell cycles and thus proliferation.[56] A clonogenic survival assay was conducted to examine whether the intracellular polymerization inhibited cancer colony formation, which is directly related to cell proliferation ability.[57] The colony numbers (14 days after the treatment) of HeLa cells treated with **PC1** or 10 min of illumination alone were 182 and 159, respectively, while polymerization resulted in a reduction of the colony number to 88 from 184 of the untreated group (Figures 3a and S32).

Key cell cycle regulators cyclin B1 and cyclin E1 were detected by immunoblotting assays. Dramatically decreased cyclin B1 and cyclin E1 expression (hardly detected) were observed indicating that the cell cycle was prohibited by the intracellular polymerization (Figure 3b).

A DNA flow cytometric assay was conducted to explore how the intracellularly generated PDMAs influence cell cycle. As shown in Figure 3c, a large proportion (46%) of cells were arrested at G2/M phases 24 h after polymerization, significantly higher than the untreated cells (20%). This increase was accompanied by reductions in G0/G1 (from 52 to 35%) and S phases (from 26 to 16%) for the "polymerized" cells when compared to the untreated cells. This observation could be attributed to the noncovalent interactions of the polymer with active biomolecules related to cell cycles, e.g., DNA and microtubules,[58,59] although this was not explored in the current study. An EdU staining assay provided further evidence for the induction of cell cycle arrest following intracellular polymerization (Figure 3d,e), i.e., polymerization resulting in a significant drop of synthesized DNA (EdU-positive cells reduced from 57 to 27% in comparison to untreated cells).

https://doi.org/10.1021/jacsau.1c00373
JACS Au 2022, 2, 579−589

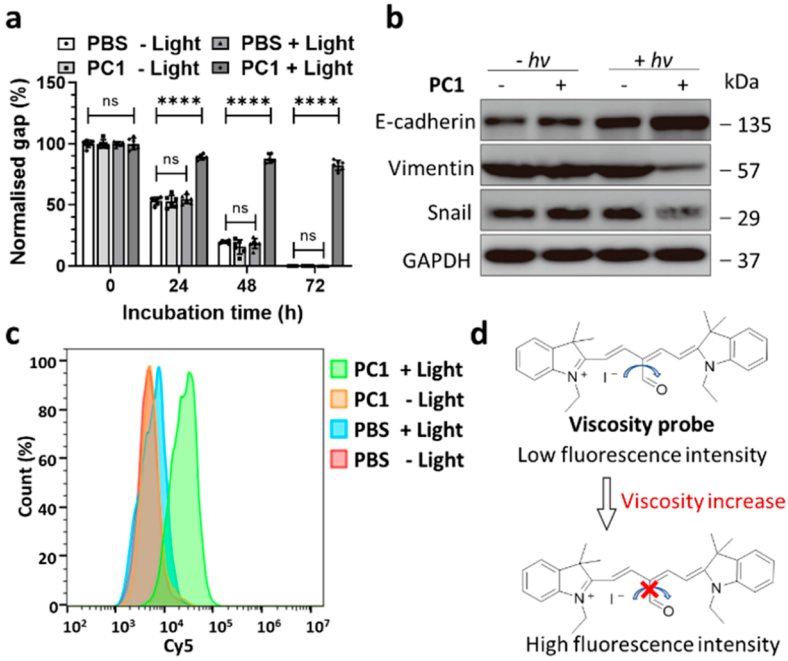

Figure 4. Exploration of the intracellular polymerization and its effect on cellular viscosity and motility. (a) Cell mobilities were determined using a wound-healing assay (n = 3). (b) Cell-motility-related proteins E-cadherin, snail, and vimentin were revealed by immunoblotting assays. (c) Cellular viscosity analyzed by flow cytometry using a Cy5-based viscosity probe. (d) Structure of the viscosity probe ($\lambda_{ex/em}$ = 640/660 nm). Statistical analysis was performed using one-way ANOVA with a Dunnett post-test compared to untreated control groups, **** $P < 0.0001$, ns (not significant).

Intracellular Polymerization Inhibits Cell Motility

A wound-healing assay was conducted with the "wound" closure monitored over 72 h (Figures 4a and S34d). The "polymerized" cells behaved very differently to the controls with the gap area essentially remaining unclosed at 89, 87, and 82% after 24, 48, and 72 h of incubation (compared to 56, 20, and 0% for the untreated cells). Key cell migration protein markers E-cadherin, snail, and vimentin were detected using immunoblotting assays (Figure 4b). A significant increase of E-cadherin and decrease of slug and vimentin were observed, indicating the inhibition of cell migration upon polymerization. These remarkable differences could be attributed to the increased cellular viscosity.[60−62]

The microviscosities of the cells were subsequently quantified using a viscosity-responsive fluorescent probe (Figures 4c,d and S34c).[63] The "polymerized" cells showed a significant increase in fluorescence intensity (6.8-fold of the untreated cells), meaning a higher cellular viscosity. Since cell cycles have been reported to be related to cellular viscosity, this would correspond to the abnormal cell cycles found in the "polymerized" cells.[64]

In Vivo Cancer Inhibition and Antimetastasis Efficacy

We explored the anticancer efficacy of this "polymeric prodrug" system in a series of animal models. The cancer inhibition efficacy was first analyzed using a HeLa tumor xenograft model (n = 6). HeLa tumor (around 100 mm^3)-bearing nude mice were randomized in groups of six animals and treated with **PC1** (1.2 mg/kg **DMA**, 600 μg/kg **CA-CTA**, and 170 μg/kg **eosin Y**) and 10 min of illumination (470 nm, 100 mW/cm^2, 2 cm above the animals) by intratumoral injections at day 0. As expected, the **PC1**-treated group without illumination did not inhibit tumor growth, and the illumination-treated group in the absence of **PC1** only resulted in moderate inhibition. When the animals were treated with both **PC1** and light, we found that tumor growth was remarkably prohibited with no obvious body weight loss (Figures 5a,b, S37, and S38).

The histological structures in the tumors were further investigated by hematoxylin and eosin (H&E) staining, TdT-mediated dUTP nick-end labeling (TUNEL), and Ki67 immunostaining (Figure 5c). Large necrotic regions were observed only in the polymerized groups, while the ratio of apoptotic cells (109 cells/mm^2, marked with red arrows) was found to be dramatically higher than that of all other groups (22, 31, and 23 cells/mm^2 for PBS-, **PC1**-, and light-treated cells, respectively, Figure 5d). Ki67 staining revealed a significant reduction in the quantity of proliferating cells (5 cells/mm^2, marked with red arrows), and thus, a reduction in tumor growth rate (25, 25, and 26 cells/mm^2 for PBS, **PC1**, and light-treated cells, respectively, Figure 5e). These are in good agreement with the *in vitro* cellular results as discussed above, i.e., the intracellular-polymerization-induced apoptosis and necroptosis and prohibited cellular proliferation.

To further investigate the long-term survival rate, a murine breast adenocarcinoma model (4T1 cell line on BALB/c mice) and a human breast adenocarcinoma model (MDA-MB-231 cell line on BALB/c nude mice) were established. The tumor (around 100 mm^3)-bearing mice were treated with or without **PC1** (injected intratumorally) and illuminated at 470 nm (4 h postinjection) at day 1. A reduced tumor growth rate was observed in the polymerization groups in both animal models, while all other control groups showed no effect (Figure 6a,b). This is exceptional as is in a fast-growing tumor model. The harvested tumors were investigated with similar results observed as for the HeLa model, i.e., tumor growth was inhibited by the intracellular polymerization by promotion of cell necroptosis, apoptosis, and lack of proliferation (Figure

https://doi.org/10.1021/jacsau.1c00373
JACS Au 2022, 2, 579−589

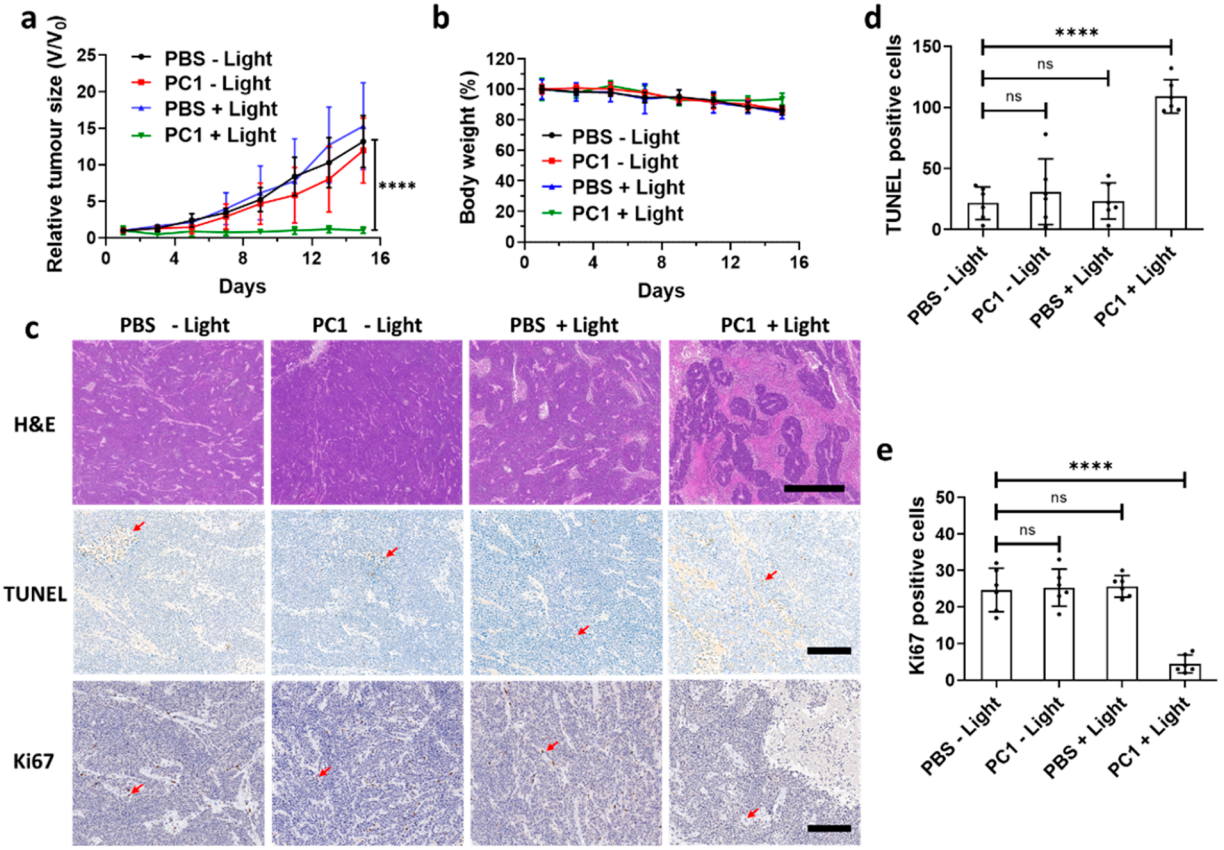

Figure 5. *In vivo* evaluation of intracellular polymerization for cancer treatment. (a) Tumor burdens and (b) body weights of HeLa-tumor-bearing Balb/c nude mice with various treatments. (c) Representative microscopic images of tumor sections are shown stained with hematoxylin/eosin (H&E), TUNEL, and Ki67, with quantified TUNEL-positive cell numbers shown in (d) and Ki67-positive cell numbers shown in (e). Scale bar = 1 mm for H&E and 200 μm for TUNEL and Ki67 (n = 6, cell numbers were counted in six random areas). Statistical analysis was performed using one-way ANOVA with a Dunnett post-test compared to untreated control groups, **** P < 0.0001, ns (not significant).

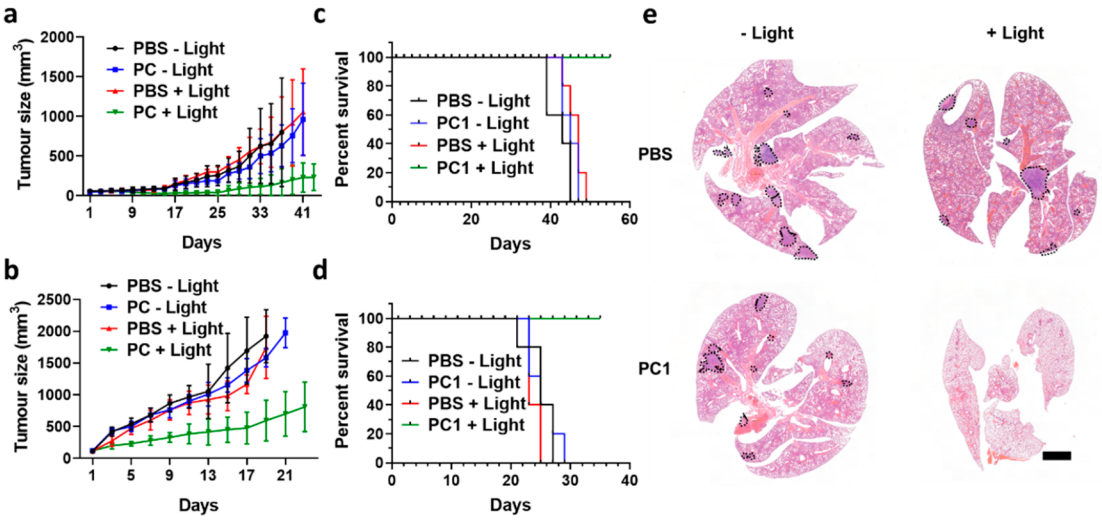

Figure 6. Survival and biosafety evaluation of intracellular polymerization. (a) Tumor burdens and (b) survival curves of MDA-MB-231-tumor-bearing BALB/c nude mice with various treatments (n = 5). (c) Tumor burdens and (d) survival curves of 4T1-tumor-bearing BALB/c mice with various treatments (n = 5). Mice were aged until moribund or the tumor volume reached 2000 mm^3. (e) Representative H&E-stained whole lung sections of each group collected from the mice on day 19. Metastatic sites were highlighted by black dash lines.

S39). The cancer treatment efficacy was also reflected by the survival study. All animals treated with the intracellular polymerization survived until the end of the studies (55 and 35 days for the MDA-MB-231 and the 4T1 models, respectively), with no survivals observed for all control groups after 49 days for the MDA-MB-231 model and 29 days for the

https://doi.org/10.1021/jacsau.1c00373
JACS Au 2022, 2, 579−589

4T1 model (Figure 6c,d). The anticancer efficacy of the "polymeric prodrug" was compared with an anticancer drug, doxorubicin, and the presynthesized **CA-PDMA-1**. Negligible tumor inhibition was found when the presynthesized **CA-PDMA-1** was intratumorally injected, where the mice treated with intratumorally injected doxorubicin or the "polymerization" strategy successfully inhibited the tumor growth (Figure S40).

To further confirm the intratumoral generation of controlled polymers, the polymers were isolated using the His-tag strategy as described previously and characterized by ^{1}HNMR and GPC (Figure S41). Identical polymer signals were observed with the molecular weight determined as 14.0 kDa ($Đ$ = 1.10). In addition, the intratumoral retention time of the fluorescent monomer, CTA, and **eosin Y** were evaluated using fluorescent monomer **YFMA** and CTA **RF-CTA**. Intense fluorescent signals and well colocations of **YFMA** and **RF-CTA** were observed in the polymerization group where 470 nm illumination was applied after the polymerization cocktail injection. Oppositely, the group without light treatment showed fewer fluorescent regions, while the CTA signals were separated from the monomer signals after 24 h (Figure S42). These data further confirmed the successful intratumoral polymerization initiated by 470 nm illumination.

It is known that the metastasis of 4T1 cells can take place in the lungs.[65] Therefore, metastasis inhibition efficacy of the intracellular polymerization was examined using the 4T1 model. 4T1-tumor-bearing BALB/c mice were treated with **PC1** and 470 nm illumination as described above. Whole lung tissues were harvested from sacrificed mice at day 19, sectioned, and stained with H&E (Figures 6e and S43). The PBS-, **PC1**-, and light-treated groups showed obvious metastasis and thus large numbers of metastatic nodules in the lungs. The doxorubicin-treated group showed minimal metastases as shown in Figure S40. A negligible sign of metastasis was observed in the polymerization group, indicating the potential of the polymerization system in inhibiting tumor metastasis.

In Vivo Biosafety Evaluation

To assess the biosafety of the "polymeric prodrug" system, body weight changes, hematological parameters, and the histological changes of major organs were examined. Initially, BALB/c mice were treated with PBS, **DMA**, **CA-CTA**, **eosin Y**, and **PC1** by subcutaneous injection and monitored over 60 days (n = 5). Negligible body weight loss was observed for all groups, indicating the low systemic toxicity of the polymerization system. This is in agreement with the tumor-bearing mice treated with the intracellular polymerization system, i.e., the body weight of the animals during the treatment period did not change drastically for the different treatments, suggesting that the treatment was tolerated, causing few side effects during the cancer therapy (Figures 5b and S41). The acute toxicity of the system was examined by monitoring the 4T1-tumor-bearing BALB/c nude mice treated with PBS, **PC1**, light, and **PC1** in the presence of light. The mice were sacrificed 48 h after the treatment, and the blood and main organs were collected and analyzed. Hematology tests showed no significant differences between any of the tested groups (Figure S44). The main organs (heart, liver, spleen, lung, and kidney) were sectioned and H&E-stained, showing no pathological abnormalities (Figure S45). These results show that the "polymeric prodrug" system does not cause acute toxicity during the cancer treatment. These results indicate that our "polymeric prodrug" has comparable anticancer efficacy to doxorubicin.

Systemic toxicity was further explored by monitoring healthy BALB/c mice treated with PBS, **DMA**, **CA-CTA**, **eosin Y**, and **PC1** subcutaneously. The blood was analyzed 48 h after treatments and the hematological biochemical markers AST, ALT (liver function), UREA, and ALP (renal function) were tested, showing no significant differences between any of the groups (Figure S46). H&E staining of main organs (heart, liver, spleen, lung, and kidney) harvested 60 days post treatment revealed no obvious physiological damage and therefore further confirmed the biosafety of the "polymeric prodrug" system in biological applications (Figure S47).

CONCLUSION

Chemotherapy is a powerful tool in the armory against cancers; however, a major limitation is global systemic toxicity. In our previous study, we demonstrated that free radical polymerization chemistry can take place within complex cellular environments, where synthetic polymers can be generated and modulate cellular functions.[26] The current study developed a controlled intracellular polymerization-based cancer therapy. The polymers were generated intracellularly in a controlled manner and significantly inhibited tumor growth by inducing cell cycle arrest, apoptosis, and necroptosis to the cancer cells while prohibiting cancer cell motility and preventing the cancer metastasis *in vitro* and *in vivo*. Importantly, the biosafety of this "polymeric prodrug" system was confirmed both in short term and in long term. Therefore, we believe that this proof-of-concept of the polymerization-chemistry-based precision medicine is a potential candidate for cancer treatment.

EXPERIMENTAL SECTION

Cell Culture

All cells were cultured in DMEM and supplemented with 10% (v/v) fetal bovine serum and penicillin/streptomycin (100 unit/mL) at 37 °C with 5% CO_2. The cells were passaged using trypsin/EDTA every 2 days.

General Procedure for Intracellular Polymerizations

Desired cells were seeded in a six-well plate at a density of 5 × 10^5 cells/well and incubated overnight. The cells were treated with the polymerization cocktail, incubated for 4 h, and washed with PBS (3×) before being illuminated at 470 nm for 10 min. The cells were incubated at 37 °C for further studies.

Histidine-Tagged Polymer Extraction and Characterization

The polymerized cells were washed with PBS three times and lysed by RIPA lysis buffer. Ni-charged Profinity IMAC resin slurry (500 μL) was transferred into a filter cartridge and washed with deionized water (3 × 5 mL) and drained. The cell lysate was diluted to 1 mL with the washing buffer (50 mM sodium phosphate, 300 mM NaCl, pH = 8.0) and added to the immobilized metal-affinity chromatography resin. The resin slurry was shaken for 30 min, the solvent drained, and the resin washed with the washing buffer (3 × 5 mL) and then treated with elution buffer (0.01 M HCl, pH = 2). The polymer solutions were collected by filtration and freeze-dried. The obtained polymer samples were analyzed by ^{1}H NMR and GPC.

In Vivo Studies

All animal experiments were performed under the Guide for Care and Use of Laboratory Animals and were approved by the Institutional Animal Care and Use Committee (IACUC) of the Shenzhen Institutes of Advanced Technology (SIAT).

https://doi.org/10.1021/jacsau.1c00373
JACS Au 2022, 2, 579−589

Polymer Extraction from Tumors

4T1-tumor-bearing mice were intratumorally injected with **DMA** (1.24 mg/kg), **His-CTA** (2.98 mg/kg), and **eosin Y** (170 μg/kg). Then, 4 h after injection, the tumor region was illuminated with 470 nm light for 10 min. The mice were sacrificed, and tumors were lysed. Polymer extractions were carried out using the same methodology as the *in vitro* study. The isolated polymers were characterized by ^{1}H NMR and GPC.

Statistical Analysis

Data were presented as mean ± SD. Dunnett's *t* tests were used to determine whether the variance between two groups is similar. One-way analysis of variance (ANOVA) was applied for comparison of multiple groups. Statistical analysis was performed using GraphPad Prism. A "*P*" value <0.05 was considered statistically significant.

■ ASSOCIATED CONTENT

Supporting Information

The Supporting Information is available free of charge at https://pubs.acs.org/doi/10.1021/jacsau.1c00373.

Materials and instruments, synthetic procedures and characterizations of new compounds, supplementary figures and text (PDF)

■ AUTHOR INFORMATION

Corresponding Author

Jin Geng − *Shenzhen Institute of Advanced Technology, Chinese Academy of Sciences, Shenzhen 518059, China;* orcid.org/0000-0003-2181-0718; Email: jin.geng@siat.ac.cn

Authors

Yichuan Zhang − *Shenzhen Institute of Advanced Technology, Chinese Academy of Sciences, Shenzhen 518059, China;* orcid.org/0000-0003-3745-0083

Quan Gao − *Shenzhen Institute of Advanced Technology, Chinese Academy of Sciences, Shenzhen 518059, China*

Weishuo Li − *Center for Molecular Metabolism, School of Environmental and Biological Engineering, Nanjing University of Science and Technology, Nanjing 210094, China*

Rongkun He − *Shenzhen Institute of Advanced Technology, Chinese Academy of Sciences, Shenzhen 518059, China*

Liwei Zhu − *Shenzhen Institute of Advanced Technology, Chinese Academy of Sciences, Shenzhen 518059, China*

Qianjin Lian − *Shenzhen Institute of Advanced Technology, Chinese Academy of Sciences, Shenzhen 518059, China*

Liang Wang − *Shenzhen Institute of Advanced Technology, Chinese Academy of Sciences, Shenzhen 518059, China*

Yang Li − *Shenzhen Institute of Advanced Technology, Chinese Academy of Sciences, Shenzhen 518059, China;* orcid.org/0000-0001-7242-4687

Mark Bradley − *EaStCHEM School of Chemistry, University of Edinburgh, Edinburgh EH9 3FJ, U.K.;* orcid.org/0000-0001-7893-1575

Complete contact information is available at: https://pubs.acs.org/10.1021/jacsau.1c00373

Author Contributions

‖These authors contributed equally: Y.Z. and Q.G.

Author Contributions

J.G. conceived, designed, and directed the project. Y.Z. conducted the compound synthesis, polymerization optimizations, polymer extraction, and characterizations. Y.Z., R.H., Q.L., and L.W. conducted the CCK-8 assays. Q.G. conducted the flow cytometry, Western blotting, and wound-healing assays. Y.Z., Q.G., and L.Z. conducted the *in vivo* experiments. Y.Z., Q.G., W.L., Y.L., M.B., and J.G. cowrote the manuscript. All authors analyzed the data and contributed to the scientific discussion and revised the manuscript.

Funding

This work was supported by the National Natural Science Foundation of China (22071263), the Natural Science Foundation of Guangdong Province, China (2020A1515010994), the Guangdong Province Zhujiang Talents Program (2019QN01Y127), the Shenzhen Fundamental Research Program (JCYJ20200109110215774), and the "Hundred Talents Program" of the Chinese Academy of Sciences (J.G.). Y.Z. acknowledges the support from the National Natural Science Foundation of China (22001261) and the China Postdoctoral Science Foundation (2020M672873, 2021T140693). Q.G. acknowledges the support from the China Postdoctoral Science Foundation (2020M682976).

Notes

The authors declare no competing financial interest.

■ ACKNOWLEDGMENTS

We thank the Platform for Science and Technology, Shenzhen Institutes of Advanced Technology, Chinese Academy of Sciences for NMR technical support.

■ REFERENCES

(1) Tang, W.; et al. A hybrid semiconducting organosilica-based O2 nanoeconomizer for on-demand synergistic photothermally boosted radiotherapy. *Nat. Commun.* **2021**, *12*, 523.

(2) Kamoun, W. S.; et al. Antitumour Activity and Tolerability of an EphA2-Targeted Nanotherapeutic in Multiple Mouse Models. *Nat. Biomed. Eng.* **2019**, *3*, 264−280.

(3) Geiger, M.; et al. Protease-activation using anti-idiotypic masks enables tumor specificity of a folate receptor 1-T cell bispecific antibody. *Nat. Commun.* **2020**, *11*, 3196.

(4) Zhang, W.; et al. Light-triggered release of conventional local anesthetics from a macromolecular prodrug for on-demand local anesthesia. *Nat. Commun.* **2020**, *11*, 2323.

(5) Sharma, A.; et al. Targeting Heterogeneous Tumors Using a Multifunctional Molecular Prodrug. *J. Am. Chem. Soc.* **2019**, *141*, 15611−15618.

(6) Zheng, Y.; et al. Enrichment-Triggered Prodrug Activation Demonstrated Through Mitochondria-Targeted Delivery of Doxorubicin and Carbon Monoxide. *Nat. Chem.* **2018**, *10*, 787−794.

(7) Jia, X.; et al. Dual Intratumoral Redox/Enzyme-Responsive NO-Releasing Nanomedicine for the Specific, High-Efficacy, and Low-Toxic Cancer Therapy. *Adv. Mater.* **2018**, *30*, 1704490.

(8) Zhou, F.; et al. Tumor Microenvironment-Activatable Prodrug Vesicles for Nanoenabled Cancer Chemoimmunotherapy Combining Immunogenic Cell Death Induction and CD47 Blockade. *Adv. Mater.* **2019**, *31*, 1805888.

(9) Cui, D.; et al. A Semiconducting Polymer Nano-prodrug for Hypoxia-Activated Photodynamic Cancer Therapy. *Angew. Chem., Int. Ed.* **2019**, *58*, 5920−5924.

(10) Kuang, S.; et al. FerriIridium: A Lysosome-Targeting Iron(III)-Activated Iridium(III) Prodrug for Chemotherapy in Gastric Cancer Cells. *Angew. Chem., Int. Ed.* **2020**, *59*, 3315−3321.

(11) Meng, T.; et al. Introduction of the α-ketoamide Structure: en Route to Develop Hydrogen Peroxide Responsive Prodrugs. *Chem. Sci.* **2019**, *10*, 7156−7162.
(12) Shao, Y.; et al. Engineering of Upconverted Metal−Organic Frameworks for Near-Infrared Light-Triggered Combinational Photodynamic/Chemo-/Immunotherapy against Hypoxic Tumors. *J. Am. Chem. Soc.* **2020**, *142*, 3939−3946.
(13) Wang, Y.; et al. Functionalized Holmium-Doped Hollow Silica Nanospheres for Combined Sonodynamic and Hypoxia-Activated Therapy. *Adv. Funct. Mater.* **2019**, *29*, 1805764.
(14) Eda, S.; et al. Biocompatibility and Therapeutic Potential of Glycosylated Albumin Artificial Metalloenzymes. *Nat. Catal.* **2019**, *2*, 780−792.
(15) Klán, P.; et al. Photoremovable Protecting Groups in Chemistry and Biology: Reaction Mechanisms and Efficacy. *Chem. Rev.* **2013**, *113*, 119−191.
(16) Castle, B. T.; Odde, D. J. Optical Control of Microtubule Dynamics in Time and Space. *Cell* **2015**, *162*, 243−245.
(17) Wang, X.; et al. Copper-Triggered Bioorthogonal Cleavage Reactions for Reversible Protein and Cell Surface Modifications. *J. Am. Chem. Soc.* **2019**, *141*, 17133−17141.
(18) Borowiak, M.; et al. Photoswitchable Inhibitors of Microtubule Dynamics Optically Control Mitosis and Cell Death. *Cell* **2015**, *162*, 403−411.
(19) Maurits, E.; et al. Immunoproteasome Inhibitor−Doxorubicin Conjugates Target Multiple Myeloma Cells and Release Doxorubicin upon Low-Dose Photon Irradiation. *J. Am. Chem. Soc.* **2020**, *142*, 7250−7253.
(20) Dadashi-Silab, S.; Doran, S.; Yagci, Y. Photoinduced Electron Transfer Reactions for Macromolecular Syntheses. *Chem. Rev.* **2016**, *116*, 10212−10275.
(21) Treat, N. J.; et al. Metal-Free Atom Transfer Radical Polymerization. *J. Am. Chem. Soc.* **2014**, *136*, 16096−16101.
(22) Mazaki, T.; et al. A Novel, Visible Light-Induced, Rapidly Cross-Linkable Gelatin Scaffold for Osteochondral Tissue Engineering. *Sci. Rep.* **2015**, *4*, 4457.
(23) Zhao, X.-X.; et al. In Situ Self-Assembled Nanofibers Precisely Target Cancer-Associated Fibroblasts for Improved Tumor Imaging. *Angew. Chem., Int. Ed.* **2019**, *58*, 15287−15294.
(24) Peng, B.; Zhao, X.; Yang, M.-S.; Li, L.-L. Intracellular Transglutaminase-Catalyzed Polymerization and Assembly for Bioimaging of Hypoxic Neuroblastoma Cells. *J. Mater. Chem. B* **2019**, *7*, 5626−5632.
(25) Niu, J.; et al. Engineering Live Cell Surfaces with Functional Polymers via Cytocompatible Controlled Radical Polymerization. *Nat. Chem.* **2017**, *9*, 537−545.
(26) Geng, J.; et al. Radical Polymerization inside Living Cells. *Nat. Chem.* **2019**, *11*, 578−586.
(27) Chen, G.; et al. Chemically Defined Conditions for Human iPSC Derivation and Culture. *Nat. Methods* **2011**, *8*, 424−429.
(28) Elsabahy, M.; Wooley, K. L. Design of Polymeric Nanoparticles for Biomedical Delivery Applications. *Chem. Soc. Rev.* **2012**, *41*, 2545−2561.
(29) Chen, M.; Zhong, M.; Johnson, J. A. Light-Controlled Radical Polymerization: Mechanisms, Methods, and Applications. *Chem. Rev.* **2016**, *116*, 10167−10211.
(30) Yeow, J.; Chapman, R.; Xu, J.; Boyer, C. Oxygen Tolerant Photopolymerization for Ultralow Volumes. *Polym. Chem.* **2017**, *8*, 5012−5022.
(31) Xu, J.; Shanmugam, S.; Duong, H. T.; Boyer, C. Organo-Photocatalysts for Photoinduced Electron Transfer-Reversible Addition−Fragmentation Chain Transfer (PET−RAFT) Polymerization. *Polym. Chem.* **2015**, *6*, 5615−5624.
(32) Keddie, D. J.; Moad, G.; Rizzardo, E.; Thang, S. H. RAFT Agent Design and Synthesis. *Macromolecules* **2012**, *45*, 5321−5342.
(33) Chiefari, J.; et al. Living Free-Radical Polymerization by Reversible Addition−Fragmentation Chain Transfer: The RAFT Process. *Macromolecules* **1998**, *31*, 5559−5562.
(34) Cornel, E. J.; van Meurs, S.; Smith, T.; O'Hora, P. S.; Armes, S. P. In Situ Spectroscopic Studies of Highly Transparent Nanoparticle Dispersions Enable Assessment of Trithiocarbonate Chain-End Fidelity during RAFT Dispersion Polymerization in Nonpolar Media. *J. Am. Chem. Soc.* **2018**, *140*, 12980−12988.
(35) Lv, C.; He, C.; Pan, X. Oxygen-Initiated and Regulated Controlled Radical Polymerization under Ambient Conditions. *Angew. Chem., Int. Ed.* **2018**, *57*, 9430−9433.
(36) Seo, M.; Hillmyer, M. A. Reticulated Nanoporous Polymers by Controlled Polymerization-Induced Microphase Separation. *Science* **2012**, *336*, 1422−1425.
(37) Miyaji, H.; Satoh, K.; Kamigaito, M. Bio-Based Polyketones by Selective Ring-Opening Radical Polymerization of α-Pinene-Derived Pinocarvone. *Angew. Chem., Int. Ed.* **2016**, *55*, 1372−1376.
(38) Ferguson, C. J.; et al. Effective ab Initio Emulsion Polymerization under RAFT Control. *Macromolecules* **2002**, *35*, 9243−9245.
(39) Gormley, A. J.; et al. An Oxygen-Tolerant PET-RAFT Polymerization for Screening Structure−Activity Relationships. *Angew. Chem., Int. Ed.* **2018**, *57*, 1557−1562.
(40) Zhang, Z.; Corrigan, N.; Bagheri, A.; Jin, J.; Boyer, C. A Versatile 3D and 4D Printing System through Photocontrolled RAFT Polymerization. *Angew. Chem., Int. Ed.* **2019**, *58*, 17954−17963.
(41) Zhang, Y.; et al. Multifunctional, Histidine-Tagged Polymers: Antibody Conjugation and Signal Amplification. *Chem. Commun.* **2020**, *56*, 13856−13859.
(42) Rautio, J.; et al. Prodrugs: Design and Clinical Applications. *Nat. Rev. Drug Discovery* **2008**, *7*, 255−270.
(43) Danial, N. N.; Korsmeyer, S. J. Cell Death: Critical Control Points. *Cell* **2004**, *116*, 205−219.
(44) Demchenko, A. P. Beyond Annexin V: Fluorescence Response of Cellular Membranes to Apoptosis. *Cytotechnology* **2013**, *65*, 157−172.
(45) Andrabi, S. A.; et al. Poly(ADP-ribose) (PAR) Polymer is a Death Signal. *Proc. Natl. Acad. Sci. U.S.A.* **2006**, *103*, 18308−18313.
(46) Pisani, C.; et al. Apoptotic and Predictive Factors by Bax, Caspases 3/9, Bcl-2, p53 and Ki-67 in Prostate Cancer after 12 Gy Single-Dose. *Sci. Rep.* **2020**, *10*, 7050.
(47) Miyashita, T.; et al. Tumor Suppressor p53 is a Regulator of bcl-2 and bax Gene Expression in vitro and in vivo. *Oncogene* **1994**, *9*, 1799−1805.
(48) Vaseva, A. V.; Moll, U. M. The Mitochondrial p53 Pathway. *Biochim. Biophys. Acta* **2009**, *1787*, 414−420.
(49) Park, E. J.; et al. β-Lapachone Induces Programmed Necrosis Through the RIP1-PARP-AIF-Dependent Pathway in Human Hepatocellular Carcinoma SK-Hep1 Cells. *Cell Death Dis.* **2014**, *5*, e1230−e1230.
(50) Artus, C.; et al. AIF promotes chromatinolysis and caspase-independent programmed necrosis by interacting with histone H2AX. *EMBO J.* **2010**, *29*, 1585−1599.
(51) Baritaud, M.; Cabon, L.; Delavallée, L.; Galán-Malo, P.; Gilles, M. E.; Brunelle-Navas, M. N.; Susin, S. A. AIF-mediated caspase-independent necroptosis requires ATM and DNA-PK-induced histone H2AX Ser139 phosphorylation. *Cell Death Dis.* **2012**, *3*, e390−e390.
(52) Sridhar, S.; Botbol, Y.; Macian, F.; Cuervo, A. M. Autophagy and Disease: Always Two Sides to a Problem. *J. Pathol.* **2012**, *226*, 255−273.
(53) Rao, S.; et al. A Dual Role for Autophagy in a Murine Model of Lung Cancer. *Nat. Commun.* **2014**, *5*, 3056.
(54) Kabeya, Y.; et al. LC3, a Mammalian Homologue of Yeast Apg8p, is Localized in Autophagosome Membranes after Processing. *EMBO J.* **2000**, *19*, 5720−5728.
(55) Mauthe, M.; et al. Chloroquine Inhibits Autophagic Flux by Decreasing Autophagosome-Lysosome Fusion. *Autophagy* **2018**, *14*, 1435−1455.
(56) Kastan, M. B.; Canman, C. E.; Leonard, C. J. P53, Cell Cycle Control and Apoptosis: Implications for Cancer. *Cancer Metastasis Rev.* **1995**, *14*, 3−15.

https://doi.org/10.1021/jacsau.1c00373
JACS Au 2022, 2, 579−589

(57) Franken, N. A. P.; Rodermond, H. M.; Stap, J.; Haveman, J.; van Bree, C. Clonogenic Assay of Cells in vitro. *Nat. Protoc.* **2006**, *1*, 2315−2319.
(58) Hamze, A.; et al. Synthesis, Biological Evaluation of 1,1-Diarylethylenes as a Novel Class of Antimitotic Agents. *ChemMedChem.* **2009**, *4*, 1912−1924.
(59) DiPaola, R. S. To Arrest or Not To G2-M Cell-Cycle Arrest. *Clin. Cancer. Res.* **2002**, *8*, 3311.
(60) Ridley, A. J.; et al. Cell Migration: Integrating Signals from Front to Back. *Science* **2003**, *302*, 1704−1709.
(61) Saadat, A.; Guido, C. J.; Shaqfeh, E. S. G. Effect of Cytoplasmic Viscosity on Red Blood Cell Migration in Small Arteriole-Level Confinements. *bioRxiv*, 2019; 572933.
(62) Trepat, X.; Chen, Z.; Jacobson, K. Cell migration. *Compr. Physiol.* **2012**, *2*, 2369−2392.
(63) Peng, X.; et al. Fluorescence Ratiometry and Fluorescence Lifetime Imaging: Using a Single Molecular Sensor for Dual Mode Imaging of Cellular Viscosity. *J. Am. Chem. Soc.* **2011**, *133*, 6626−6635.
(64) Teng, Y.; Zhu, K.; Xiong, C.; Huang, J. Electrodeformation-Based Biomechanical Chip for Quantifying Global Viscoelasticity of Cancer Cells Regulated by Cell Cycle. *Anal. Chem.* **2018**, *90*, 8370−8378.
(65) Sui, J.; et al. Acid-Labile Polysaccharide Prodrug via Lapatinib-Sensitizing Effect Substantially Prevented Metastasis and Post-operative Recurrence of Triple-Negative Breast Cancer. *Nanoscale* **2020**, *12*, 13567−13581.

https://doi.org/10.1021/jacsau.1c00373
JACS Au 2022, 2, 579−589